CrystEngComm

PAPER

View Article Online
View Journal | View Issue

Cite this: *CrystEngComm*, 2020, **22**, 6911

One-step surfactant-free controllable synthesis and tunable up-conversion/down-shifting white light emissions of Sr_2YF_7 crystals doped with Ln^{3+} ions†

Dingyi Shen,[a] Yini Mao,[a] Jun Yang,[a] Lu Cao,[b] Juntao Ning[b] and Shanshan Hu*[a]

Received 26th February 2020,
Accepted 20th September 2020

DOI: 10.1039/d0ce00280a

rsc.li/crystengcomm

In this work, uniform and monodisperse Sr_2YF_7 spheres were successfully synthesized *via* a facile one-step hydrothermal route without employing any surfactant. Particularly, a well-defined morphology of Sr_2YF_7 crystals ranging from spherical to octahedral shape was first achieved by adjusting the pH values. In addition, the spherical products doped with 6% Ln^{3+} (Ln = La, Ce, Pr, Sm, Gd, and Dy) show different sizes ranging from 300 to 600 nm. The Sr_2YF_7 crystals also exhibit excellent multicolor DS/UC luminescence properties after doping with different Ln^{3+} ions. Energy transfer from Tb^{3+} to Eu^{3+} was observed in Sr_2YF_7 crystals; the Sr_2YF_7:Dy^{3+} crystals showed nearly white light emission under UV excitation; Sr_2YF_7:Yb^{3+}/Er^{3+}/Tm^{3+} crystals could produce pure white light with a CIE color coordinate of (0.3123, 0.3005) by controlling the doping concentrations of Er^{3+} and Tm^{3+} ions under 980 nm excitation. The as-prepared phosphors may potentially serve as light, color displays and markers in biological imaging.

1 Introduction

Nowadays, inorganic rare earth (RE) materials doped with trivalent lanthanide ions (Ln^{3+}) are drawing attention greatly because of their wide application in various devices such as white light-emitting diodes,[1] solid-state lasers,[2] solar cells,[3] and sensors.[4] Among the many inorganic rare earth luminescent matrix materials,[5–7] rare earth fluoride is of particular interest due to its toxicity-free nature and high stability compared to some organic dyes and semiconductor quantum dots,[8,9] as well as its utmost efficiency for up-conversion emission.[10] It is well known that fluoride materials have low lattice phonon energy to effectively reduce phonon-assisted nonradiative relaxation according to theoretical calculations.[11]

Thus far, there have been several approaches to prepare RE-based fluorides with controllable phases, morphologies and chemical compositions.[12] The three most common methods are thermal decomposition, high-temperature coprecipitation and hydro(solvo)-thermal synthesis, respectively. However, the first two ways may also bring some inevitable problems like complex experimental conditions, pollution and safety concerns[13–15] despite high manufacturing yields. It seems that the hydrothermal method suits better to gain highly crystalline fluoride materials under relatively mild conditions (convenient, simple and environment-friendly). Generally, surfactants were employed to control the morphology and shapes during the preparation of materials by a wet chemical method. In fact, it is difficult to remove the residual surfactants entirely and they may even further affect the phosphors' luminous quenching centers and luminescence properties.[16] Therefore, it is of significant importance to find a proper way to simplify the synthetic process of RE-based fluorides without any additives in the premise of desirable results.

Up to now, much effort has been made for the synthesis of RE-based fluorides (RE = Y, La, Ce, Pr, Nd, Sm, Eu, Gd, Tb, Dy, Ho, Er, Tm, Yb and Lu) with controllable crystalline phases, shapes and sizes.[17–20] In the family of Y^{3+}-based fluorides, except for $NaYF_4$,[21] YOF,[22] $LiYF_4$ (ref. 23) and $BaYF_5$,[24] Sr_2YF_7, as an important matrix for Ln^{3+} ions to fabricate up-conversion (UC) or down-shifting (DS) phosphors, has aroused much research interest. Recently, Chen's group has reported Sr_2YF_7:Ln^{3+} nanoparticles for biodetection by a thermal decomposition method;[20] Xia has prepared Sr_2LnF_7:Yb^{3+}, Er^{3+} (Ln = Y, Gd) nanocrystals by an EDTA-assisted method;[25] Ma reported ultrasmall face-centered cubic Sr_2YF_7:Yb^{3+}, Er^{3+}/Yb^{3+}, Tm^{3+} nanocrystals under the condition of oleic acid;[26] Han's group has also made the hierarchical microspheres Sr_2YF_7:Eu^{3+} by a

[a] *School of Chemistry and Chemical Engineering, Southwest University, Chongqing 400715, China. E-mail: hushan3@swu.edu.cn*
[b] *Chongqing Songshuqiao Middle School, Chongqing 401147, China*

† Electronic supplementary information (ESI) available. See DOI: 10.1039/d0ce00280a

hydrothermal method.[27] Although several attempts have been made for the synthesis of Ln^{3+}-doped Sr_2YF_7, only color emissions were produced, as previously reported in the literature. To date, a systematic survey on the optical properties, in particular UC and DS white light emission of Ln^{3+} in the Sr_2YF_7 host, is still lacking. To gain deep insights into the understanding of the electronic structure and optical properties (in particular, white light emission) of Ln^{3+} ions in the Sr_2YF_7 host is of vital importance for optimizing their optical performance for potential applications.

Here, we produced uniform and monodisperse Sr_2YF_7:Ln^{3+} microcrystals by a facile one-pot hydrothermal approach without any surfactant. The morphologies and sizes of the Sr_2YF_7 microcrystals could be easily adjusted by doping with different Ln^{3+} ions and changing the pH values. We performed a study of multi-doping Ln^{3+} ions in the Sr_2YF_7 host. The prepared Sr_2YF_7:Ln^{3+} (Ln = Dy, Tb, Eu, Yb, Er, Tm) phosphors showed tunable DS/UC luminescence properties. Specifically, we first found the energy transfer of $Tb^{3+} \rightarrow Eu^{3+}$ and obtained white light emission of tri-doped Yb^{3+}–Er^{3+}–Tm^{3+} in the Sr_2YF_7 host, respectively.

2 Experimental section

Chemicals

RE_2O_3 (RE = Yb, Er, Ho, Dy, Gd, Eu, Sm and La) (99.99%), $Ce(NO_3)_3$ (99.99%), Tb_4O_7 (99.99%) and Pr_6O_{11} (99.99%) were acquired from Goring High-tech Material Corporation Limited (China). Strontium chloride ($SrCl_2$), sodium tetrafluoroborate ($NaBF_4$), sodium hydroxide (NaOH), and hydrochloric acid (HCl) were purchased from Aladdin Industrial Corporation (China) and used without further purification. $RECl_3$ (RE = Yb, Er, Ho, Dy, Tb, Gd, Eu, Sm, Pr and La) were prepared by dissolving the corresponding rare earth oxides in dilute HCl and then evaporating the excess HCl.

Synthesis

In a typical synthesis for the preparation of the Sr_2YF_7 host, 2 mmol $SrCl_2$, 1 mmol YCl_3 solution and 30 mL deionized water were added together to form a transparent solution by stirring in a 100 mL beaker for 15 minutes. Subsequently, 8 mmol $NaBF_4$ was added dropwise into the above solution under vigorous stirring. The pH was adjusted to the required value by adding 1 mol L^{-1} NaOH solution dropwise. The volume of the system was finally maintained at 35 mL. After the process of enough stirring, the obtained solution was transferred into a Teflon bottle held in a stainless steel autoclave, sealed and kept at 220 °C for 24 h, and then cooled to room temperature naturally. The final products were centrifuged, washed several times with deionized water and ethanol, and then dried at 80 °C for 12 h. Other samples (Sr_2YF_7:Ln^{3+}) were synthesized by a similar method except for using different stoichiometric ratios of rare earth ions.

Characterization

Powder X-ray diffraction (XRD) measurements were performed using a Purkinje Genera Instrument MSALXD3 under the condition of Cu Kα radiation (λ = 0.15406 nm) at a scanning rate of 8° min^{-1} from 20° to 70° with 2θ, 20 mA and 36 kV. The morphology and energy-dispersive spectrometry of the samples were inspected using a field emission scanning electron microscope (FE-SEM, XL30, Philips) operating at an accelerating voltage of 10 kV. The DS PL measurements were conducted using a Hitachi F-7000 spectrophotometer equipped with a 150 W xenon lamp as the excitation source. The UC PL measurements were carried out using a 980 nm laser with MDL-N-980-8W as the excitation source. The luminescence decays were recorded using an FLSP920 fluorescence spectrophotometer and a Shimadzu R9287 photomultiplier (200–900 nm) accompanied by a liquid nitrogen-cooled InGaAs (800–1700 nm) diode as the detector. All the measurements were performed at room temperature.

3 Results and discussion

3.1. Phase identification and morphology of Sr_2YF_7 hosts

Sr_2YF_7 has a tetragonal crystal structure with a space group of *I*4/*mcm* ($a = b$ = 11.416 Å, c = 13.291 Å and Z = 10). As shown in Fig. 1a, the well-defined diffraction peaks of the obtained products can fit well with the standard data of Sr_2YF_7 (JCPDS no. 53-0675). The crystallite size of the samples

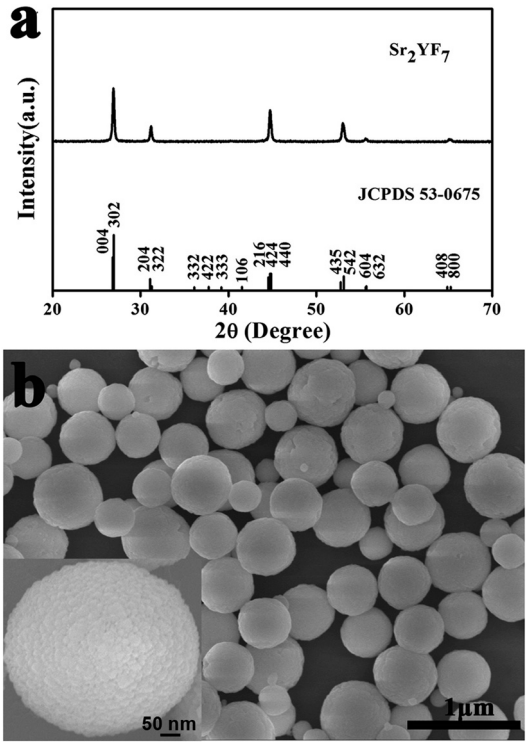

Fig. 1 XRD pattern (a) and SEM image (b) of the as-synthesized Sr_2YF_7 host under the conditions of $Sr^{2+}/Y^{3+}/BF_4^-$ = 2 : 1 : 8 and pH = 3. Sr_2YF_7 has the stoichiometric ratio of Sr : Y : F = 2 : 1 : 7, so we use excess $NaBF_4$ to get pure-phase Sr_2YF_7 products.

can be estimated from the Scherrer equation, $D = 0.941\lambda/\beta\cos\theta$, where D is the average grain size, the factor 0.941 is characteristic of spherical objects, λ is the X-ray wavelength (0.15405 nm), and θ and β are the diffraction angle and full-width at half-maximum (FWHM, in radian) of an observed peak, respectively. The strongest peaks (302) at $2\theta = 26.976°$ were used to calculate the average crystallite size (D) of the Sr_2YF_7 host. The estimated average crystallite size is about 26 nm.

The SEM indicates that the morphology of products shows uniform and monodisperse spheres with a diameter of 500 nm, as shown in Fig. 1b. Moreover, the high-magnification SEM image (inset of Fig. 1b) clearly shows that the obtained product is polycrystalline,[28,29] as it further actually consists of many smaller grains with a size of 20–40 nm. The size is basically in agreement with the results estimated from the above-mentioned Scherrer equation (26 nm). Because smaller nanograins contribute more to the broadening of the diffraction peaks, the average nanocrystal size estimated from the Scherrer equation is smaller than that determined from the SEM topology in the case of Sr_2YF_7 spheres.[30] The barely low agglomeration of spherical particles are beneficial for practical applications like form coating and ceramic. Generally speaking, the phase and morphology of nano/micromaterials not only depend on the aimed compounds' intrinsic structures but also involve many experiment factors like types of raw materials, pH values, doping ions, temperatures and reaction times. Here, we used $NaBF_4$ as a F^- source and kept the other conditions unchanged (temperature, reaction time and free-surfactant). The effects of pH values and various doping rare earth ions on the phase/morphology of crystals are discussed in detail next.

3.1.1. Effect of pH on the phase and morphology. To study the role that pH plays in the system, we add sodium hydroxide (NaOH) to change the pH of the initial solution under the other same condition. Fig. 2 illustrates the typical XRD patterns of Sr_2YF_7 samples with different pH values.

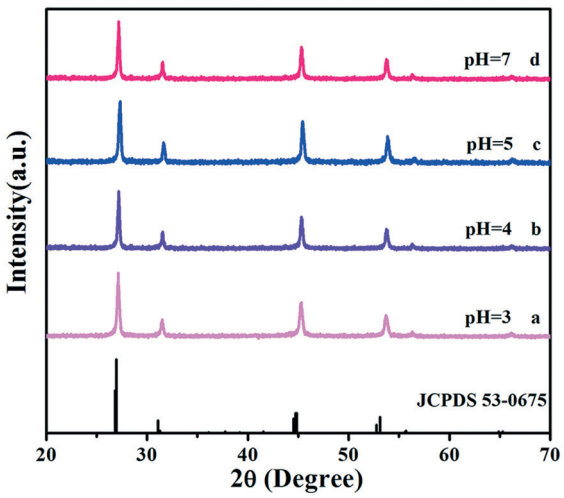

Fig. 2 XRD patterns of the Sr_2YF_7 host with different pH values.

Compared with the standard peaks, no other diffraction peaks are detected and all the diffraction peaks of the as-prepared Sr_2YF_7 particles are barely shifted. The more significantly important thing is the high crystallinity, which usually suggests less defects and stronger luminescence.

To precisely analyse the influence of pH values on the morphological evolution, the SEM images are provided in Fig. 3. First, the pH is 3 during the process of preparation. As shown in Fig. 3a, the original Sr_2YF_7 host consists of numerous uniform and monodisperse spheres whose surfaces are consisting of many smaller grains with a size of 20–40 nm (Fig. 1b). When the pH was adjusted to 4 (Fig. 3b), it was obvious that the morphology of crystals remained unchanged, which implied the coexistence of sphere-like and octahedron-like shapes. The shapes were assembled by many rhombus-like nanoparticles, showing a faceted morphology.[31] Small particles have high surface energy and the nanoparticles quickly aggregate together to reduce the energy.[32,33] Upon further addition of NaOH to the solution (pH = 5), the morphologies of the obtained crystals all converted into octahedral shapes (Fig. 3c). At pH = 7, most of the octahedral shapes become larger and some even combination of polyhedral structures (Fig. 3d). The schematic of the morphological evolution can be seen in Fig. 3e.

By continuously increasing the pH value, abnormal phase transition occurs and the resulting product consists of many smaller nanoparticles forming irregular aggregations. Thus, we can infer that various pH values are the key elements influencing the morphology and phase of the final products. During the synthetic process, F^- ions are released from the hydrolysis of $NaBF_4$:

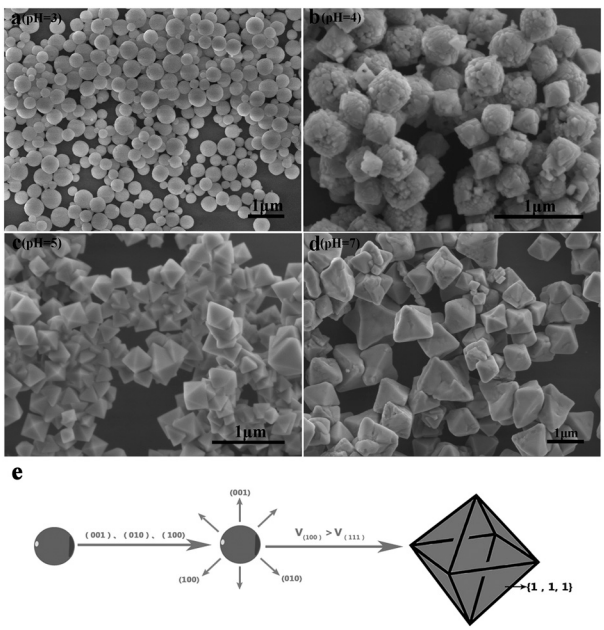

Fig. 3 SEM images of Sr_2YF_7 crystals prepared at different pH values: (a) pH = 3, (b) pH = 4, (c) pH = 5, and (d) pH = 7. Schematic of the morphological evolution (e).

$$BF_4^- + 3H_2O \rightarrow 3HF + F^- + H_3BO_3$$

The high pH values increase the concentration of F^- ions in the solution, which affect the rate of crystal nucleation and crystal growth.[32] By adding OH^- ions into the solution to adjust the pH, the nucleation rate could be changed owning to the competition of OH^- ions and F^- ions. With the increase in OH^- ions, the unavoidable chelation between OH^- anions and Y^{3+}/Sr^{2+} cations takes place, thus inhibiting the integration between F^- ions and Y^{3+}/Sr^{2+} ions to get larger crystals by kinetics.[34] Some researchers have also investigated that Na^+ ions may be selectively absorbed on the different crystal facets of nanoparticles, leading to different shapes.[35] In summary, the pH values of the initial solution can effectively change the balance between the ion transport rates and chemical potential, and then affect the crystal orientation.[36] Based on these analysis results, the size- and morphology-controllable Sr_2YF_7 nanocrystals can be effectively synthesized by a facile one-pot hydrothermal approach without surfactants.

3.1.2. Effect of doping Ln^{3+} on the phase and morphology. It has been investigated that the size and shape of alkaline earth-rare earth fluorides can be modified by doping Ln^{3+} ions.[27,37] Here, the Sr_2YF_7:6% Ln^{3+} (Ln = La, Ce, Pr, Sm, Gd and Dy) crystals have already been prepared and Fig. 4 displays the XRD results of these samples. All diffraction peaks of Sr_2YF_7:6% Ln^{3+} (Ln = La, Ce, Pr, Sm, Gd and Dy) can be readily indexed to the pure tetragonal phase of Sr_2YF_7 (space group: *I*4/*mcm*) according to the JCPDS file no. 53-0675. No additional peaks of other phases have been found, indicating that the Ln^{3+} ions are effectively built into the Sr_2YF_7 host lattice. Moreover, the characteristic diffraction peak corresponding to the (302) crystal plane has a slight shift toward the low 2θ direction after doping the Ln^{3+} ions (seeing dot line in Fig. 4), which reveals that Ln^{3+} ions were successfully incorporated into the crystal lattice of Sr_2YF_7 crystals and occupied the position of the original Y^{3+} ions. The ionic radii of Y^{3+} and Dy^{3+}–La^{3+} are 0.9 Å and 0.97–1.1 Å, respectively. Therefore, Ln^{3+} ion dopants (Ln = La, Ce, Pr, Sm, Gd and Dy) are expected to occupy Y^{3+} sites because of a similar ionic radius and valence.[10] However, when the Y^{3+} ions are replaced with Dy^{3+}–La^{3+}, the unit cell volume becomes larger, which is visually expressed as the diffraction peak shifts to a lower 2θ degree from Dy^{3+} to La^{3+} ions.[38]

The doped Ln^{3+} ions indeed make some subtle differences in the host.[37] This is the reason that the obtained monodisperse spheres of Sr_2YF_7 in the presence of 6% doped Ln^{3+} ions become bigger from La^{3+} to Dy^{3+} (Fig. 5). Once the lanthanide dopants from La^{3+} to Dy^{3+} with a radius ranging from 1.1 Å to 0.97 Å were mixed into the crystal lattice of Sr_2YF_7, the size of the Sr_2YF_7 microspheres composed of nanoparticles was remarkably changed with an average diameter ranging from 300 nm to 600 nm (Fig. S1†). In fact, the substitution of Y^{3+} ions with Ln^{3+} ions with a larger radius could decelerate the anisotropic crystalline growth, and the electron charge density of surface relevantly increases, which can substantially slow the diffusion rate of F^- ions towards the surface of the rare-earth fluoride crystal nuclei as a result of charge repulsion.[28,39]

3.2. Luminescence properties

After investigating the effect of pH values and doped Ln^{3+} ions on the morphology and phase of the Sr_2YF_7 host, it was reported that Sr_2YF_7 is an excellent host to contain various rare earth ions for rich luminescence. Herein, we are devoted to the DS/UC luminescence properties including Dy^{3+}, Tb^{3+} and Eu^{3+} single-doped, Tb^{3+}/Eu^{3+}, Yb^{3+}/Er^{3+} and Yb^{3+}/Tm^{3+} co-doped and $Yb^{3+}/Er^{3+}/Tm^{3+}$ tri-doped in the Sr_2YF_7 host.

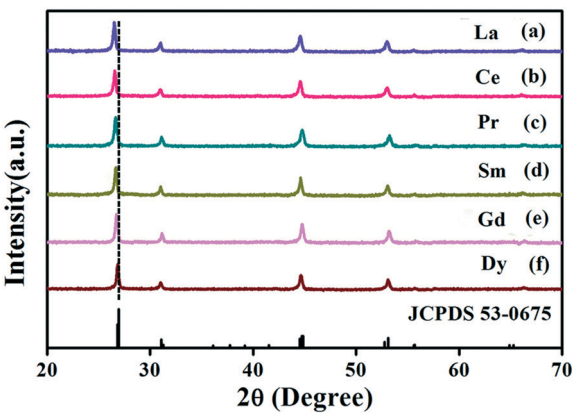

Fig. 4 XRD patterns of Sr_2YF_7:6% Ln^{3+}.

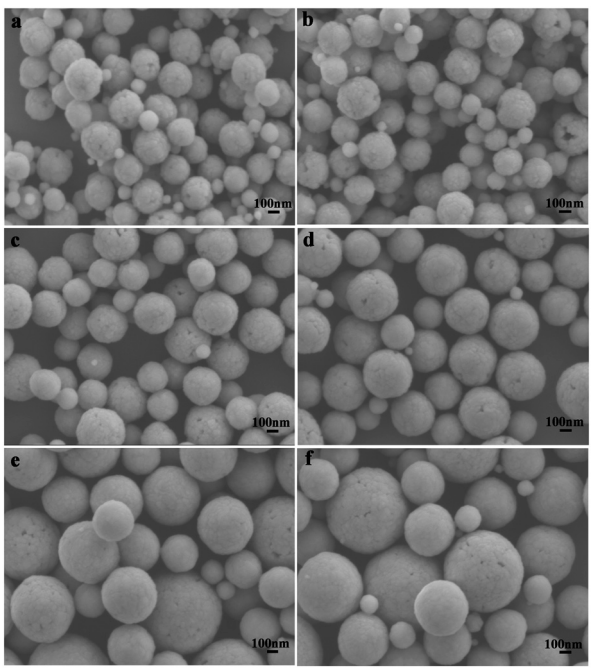

Fig. 5 SEM images of Sr_2YF_7 doped with different Ln^{3+} ions: (a) 6% La^{3+}, (b) 6% Ce^{3+}, (c) 6% Pr^{3+}, (d) 6% Sm^{3+}, (e) 6% Gd^{3+} and (f) Dy^{3+}, respectively.

We used solid samples for all the luminescence measurements at room temperature.

3.2.1. DS photoluminescence. The Eu^{3+} ion is one of the most excellent red-emitting activators in rare-earth ion-doped commercial phosphors due to its dominant transition in the red spectral area. The Sr_2YF_7:10% Eu^{3+} crystals are selected as a representative example to show its PL properties. As shown in Fig. 6a, the excitation spectrum (monitored at 595 nm) consists of several narrow peaks, which are the Eu^{3+} characteristic f–f transitions (318 nm, $^7F_0 \rightarrow {}^5H_6$; 362 nm, $^7F_0 \rightarrow {}^5D_4$; 382 nm, $^7F_0 \rightarrow {}^5G_2$; 394 nm, $^7F_0 \rightarrow {}^5L_6$, strongest one; 465 nm, $^7F_0 \rightarrow {}^5D_2$) of its $4f^6$ configurations. In addition, the characteristic emissions (excited at 394 nm) result from the transitions of $^5D_{0,1} \rightarrow {}^7F_J$ (J = 1, 2, and 3) including $^5D_1 \rightarrow {}^7F_3$ (558 nm), $^5D_0 \rightarrow {}^7F_1$ (595 nm) and $^5D_0 \rightarrow {}^7F_2$ (620 nm). Moreover, it is quite obvious that the emission centered at 595 nm belonging to the $^5D_0 \rightarrow {}^7F_1$ magnetic dipole transition is stronger than 620 nm belonging to the $^5D_0 \rightarrow {}^7F_2$ electric dipole transition, indicating that the Eu^{3+} ions are encased in a high symmetric environment according to the Judd–Ofelt theory.[40] Therefore, Eu^{3+} ions are often applied to study the local site characteristics as a structure probe.[41] From Fig. 6b, the emission intensities of Eu^{3+} rapidly increase with the increase in doping concentration and reaches a maximum at x = 10, and then slowly decreases due to concentration quenching. With the increase in concentration of Eu^{3+} ions, the resonance energy transfer is allowed because the distance of the luminescent centers becomes short enough to bring about the energy transfer from one luminescent center to another. Therefore, the concentration quenching of Eu^{3+} ions takes place when the concentration of Eu^{3+} ions increases to a high enough level.

To find the optimum doping concentration (doping concentration when the sample shows the highest emission) in $Sr_2YF_7:Tb^{3+}$ and $Sr_2YF_7:Dy^{3+}$, different results are given in

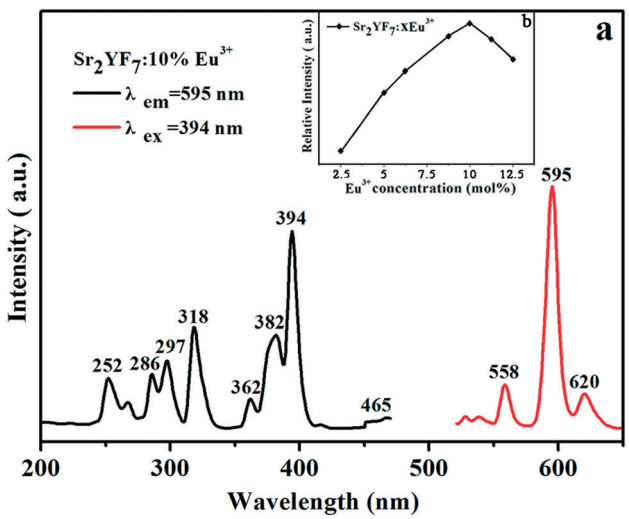

Fig. 6 PL excitation (left) and emission (right) spectra of Sr_2YF_7:10% Eu^{3+} (a) and PL emission intensity at 595 nm with different Eu^{3+} concentrations (b).

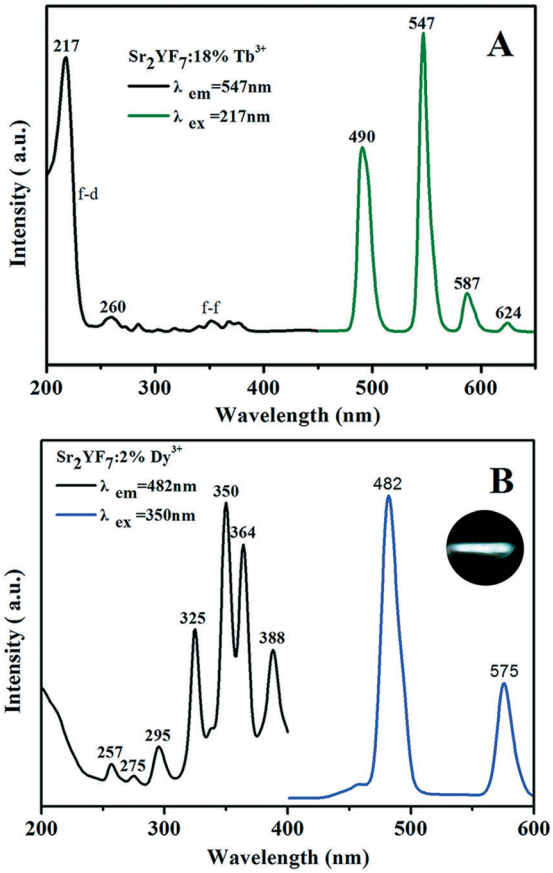

Fig. 7 PL excitation (left) and emission (right) spectra of Sr_2YF_7:18% Tb^{3+} (A) and Sr_2YF_7:2% Dy^{3+} (B), respectively. In addition, the luminescence photo of the Sr_2YF_7:2% Dy^{3+} crystals under excitation at 350 nm UV light (illustration in B).

Fig. S2.† Fig. 7A displays the PL spectra of the acquired Sr_2YF_7:18% Tb^{3+} phosphors. When monitored with the 547 nm emission of Tb^{3+} ($^5D_4 \rightarrow {}^7F_5$), the excitation spectrum consists of a strong band with maximum at 217 nm in the range of 200–300 nm and several weak peaks in the range of 300–400 nm, corresponding to the spin-allowed f → d transition and f → f transitions of Tb^{3+} ions, respectively. Under 217 nm UV excitation, the emission spectrum exhibits the $^5D_4 \rightarrow {}^7F_j$ (j = 3, 4, 5, 6) transitions of Tb^{3+} ions. Four narrow peaks centered at 490 nm, 547 nm, 587 nm and 624 nm, originating from $^5D_4 \rightarrow {}^7F_6$ (490 nm) in the blue region, $^5D_4 \rightarrow {}^7F_5$ (547 nm) in the green region, and $^5D_4 \rightarrow {}^7F_4$ (587 nm) and $^5D_4 \rightarrow {}^7F_3$ (624 nm) in the red region. Apparently, the $^5D_4 \rightarrow {}^7F_5$ transition at 547 nm is the dominant peak. For the Sr_2YF_7:2% Dy^{3+} sample (Fig. 7B), it can be easily seen that there are several sharp excitation bands at 325 nm, 350 nm, 364 nm and 388 nm, corresponding to the transitions of Dy^{3+} ions ($^6H_{15/2} \rightarrow {}^6P_{3/2}$, $^6P_{7/2}$, $^6P_{5/2}$, $^4F_{7/2}$). Upon excitation at 350 nm, the as-prepared Sr_2YF_7:2% Dy^{3+} phosphors show nearly white emission when viewed with naked eyes (illustration in Fig. 7B). The emission spectrum consists of two main peaks at 482 nm and 575 nm, which are ascribed to the magnetic dipole ($^4F_{9/2} \rightarrow {}^6H_{15/2}$) and electric dipole transitions ($^4F_{9/2} \rightarrow$

$^6H_{13/2}$) of Dy^{3+} ions, respectively.[42] Just like Eu^{3+} $^5D_0$–$^7F_2$, the Dy^{3+} $^4F_{9/2}$–$^6H_{13/2}$ emission belongs to hypersensitive transitions with $\Delta J = 2$, which is strongly influenced by the surrounding environment. When Dy^{3+} is located at a lower-symmetry local site, this emission transition will be stronger in its emission spectra.[43–45] Here, the former ($^4F_{9/2} \rightarrow {}^6H_{15/2}$) is stronger than the latter ($^4F_{9/2} \rightarrow {}^6H_{13/2}$), indicating that Dy^{3+} ions are located in a high symmetrical chemical environment just like Eu^{3+} ions in the host.[43–45]

On the basis of doping Tb^{3+} and Eu^{3+} ions separately in the Sr_2YF_7 host, next we attempt to dope Tb^{3+} and Eu^{3+} ions simultaneously in the sample (Fig. 8). The PL spectra of Sr_2YF_7:12% Tb^{3+} (Fig. 8a) and Sr_2YF_7:6% Eu^{3+} (Fig. 8b) both contain the characteristics of Tb^{3+} and Eu^{3+} ion peaks, respectively. However, when doping 6% Eu^{3+} ions in Sr_2YF_7:12% Tb^{3+}, the spectrum of Sr_2YF_7:12% Tb^{3+}/6% Eu^{3+} sample presents significant difference, as shown in Fig. 8c. Under monitoring at 594 nm of Eu^{3+} ions in Fig. 8c, the main excitation peaks are just like that in Fig. 7a except from a few weak transition lines of Eu^{3+} ions at 318 nm ($^7F_0 \rightarrow {}^5H_6$), 362 nm ($^7F_0 \rightarrow {}^5D_4$), 382 nm ($^7F_0 \rightarrow {}^5G_2$) and 394 nm ($^7F_0 \rightarrow {}^5L_6$), respectively. It is worthwhile to notice that the co-doped emission spectrum (λ_{ex} = 217 nm) consists of not only the narrow peaks of Tb^{3+} ions at 490 nm ($^5D_4 \rightarrow {}^7F_6$) and 547 nm ($^5D_4 \rightarrow {}^7F_5$) but also the narrow peaks of Eu^{3+} ions at 594 nm ($^5D_0 \rightarrow {}^7F_1$) and 620 nm ($^5D_0 \rightarrow {}^7F_2$). Analyzing the results shown in Fig. 8c, the presence of the excitation bands and lines of Tb^{3+} (217 nm) in the excitation spectrum monitored with Eu^{3+} emission (594 nm) clearly indicates that an energy transfer has occurred from Tb^{3+} to Eu^{3+} in the Sr_2YF_7:12% Tb^{3+}/6% Eu^{3+} sample.[46–51] Since excited at 217 nm of Tb^{3+}, the emission spectrum also exists the peaks of Eu^{3+} ions centered at 594 and 620 nm besides the peaks of Tb^{3+} ions, also suggesting clearly that the energy transfer from Tb^{3+} to Eu^{3+} has occurred in the Sr_2YF_7:12% Tb^{3+}/6% Eu^{3+} sample.[46–51]

As we all know, the acceptor has no influence on the decay time of a donor when the radiative energy transfer processes are dominating in certain materials. However, the acceptor has a great influence on the decay time of a donor when the nonradiative energy transfer processes are dominating. With the increase in the concentration of acceptors, the decay time of the donor decreases gradually. Similar to the double exponential luminescence decay of Tb^{3+} in the Sr_2YF_7:12% Tb^{3+} sample, the luminescence decay curve of Tb^{3+} in the Sr_2YF_7:12% Tb^{3+}/6% Eu^{3+} sample can also be well fitted into a double exponential function (Fig. 9). In addition, the life time τ for the $^5D_4$ state of Tb^{3+} is determined to be 0.228 ms in the Sr_2YF_7:12% Tb^{3+}/6% Eu^{3+} sample, which is much shorter than that in the Sr_2YF_7:12% Tb^{3+} (0.559 ms) sample. Obviously, the shortening of the life time in Sr_2YF_7:12% Tb^{3+}/6% Eu^{3+} with respect to Sr_2YF_7:12% Tb^{3+} is due to the occurrence of the energy transfer from Tb^{3+} to Eu^{3+} in the former sample.[46–51]

3.2.2. UC photoluminescence. To achieve multicolor emission as much as possible, the UC photoluminescence of Sr_2YF_7 crystals doped with the Yb^{3+}/Er^{3+}, Yb^{3+}/Tm^{3+} and Yb^{3+}/Er^{3+}/Tm^{3+} ions were investigated under 980 nm excitation, whereas the result of Sr_2YF_7:1% Er^{3+} shows the strongest green light by adjusting the single-doped concentration of Er^{3+} ions; we subsequently fixed the 1 mol% Er^{3+} ion concentrations to vary the concentrations of Yb^{3+} from 5 mol% to 20 mol%, as shown in Fig. 10A. It was found that the optimum concentration of Yb^{3+} ions is 15 mol%. The emission spectrum of Sr_2YF_7:15% Yb^{3+}/1% Er^{3+} consists of four emission peaks. The weak violet emission centered at 408 nm is assigned to the $^2H_{9/2}$–$^4I_{15/2}$ of Er^{3+}.[52,53] The dominant emissions centered at 522/540 nm in the green region and a red emission centered at 652 nm, which are assigned to the $^2H_{11/2} \rightarrow {}^4I_{5/2}$, $^4S_{3/2} \rightarrow {}^4I_{5/2}$ and $^4F_{9/2} \rightarrow {}^4I_{5/2}$ transitions of Er^{3+} ions, respectively.[26,54] The green emissions of $^2H_{11/2} \rightarrow {}^4I_{5/2}$ and $^4S_{3/2} \rightarrow {}^4I_{5/2}$ are much stronger than the red emissions of $^4F_{9/2} \rightarrow {}^4I_{5/2}$. In addition, the sample presented vivid green slightly yellow when viewed with naked eyes. As the Sr_2YF_7:15% Yb^{3+}/y% Tm^{3+} phosphors indicated in Fig. 10B, the proper concentration of Tm^{3+} ions is 0.5 mol% under 980 nm excitation. Additionally, the Sr_2YF_7:15%

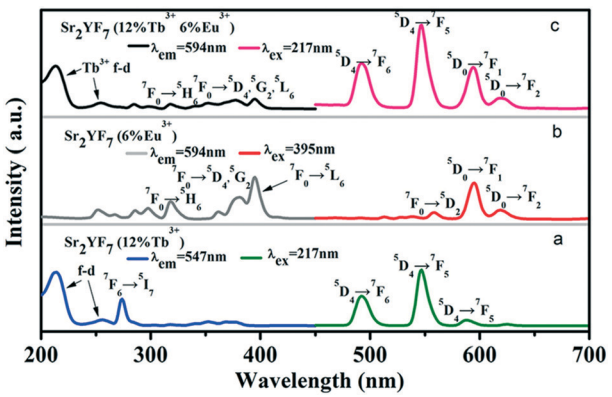

Fig. 8 PLE and PL spectra of Sr_2YF_7:12% Tb^{3+} (a), Sr_2YF_7:6% Eu^{3+} (b) and Sr_2YF_7:12% Tb^{3+}/6% Eu^{3+} (c) crystals.

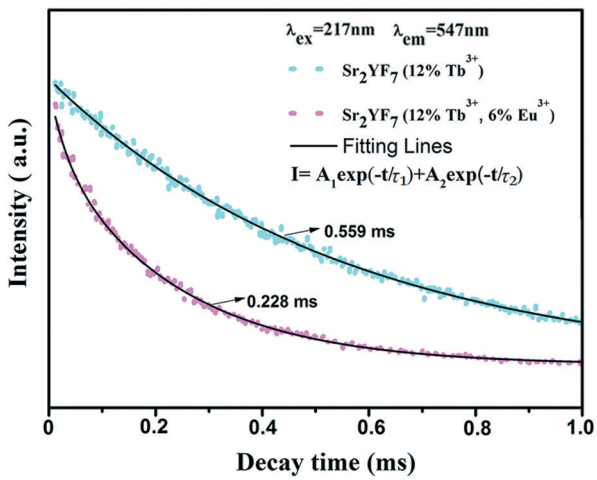

Fig. 9 Decay curves for the luminescence of Tb^{3+} in Sr_2YF_7:12% Tb^{3+} and T Sr_2YF_7:12% Tb^{3+}/6% Eu^{3+}, respectively.

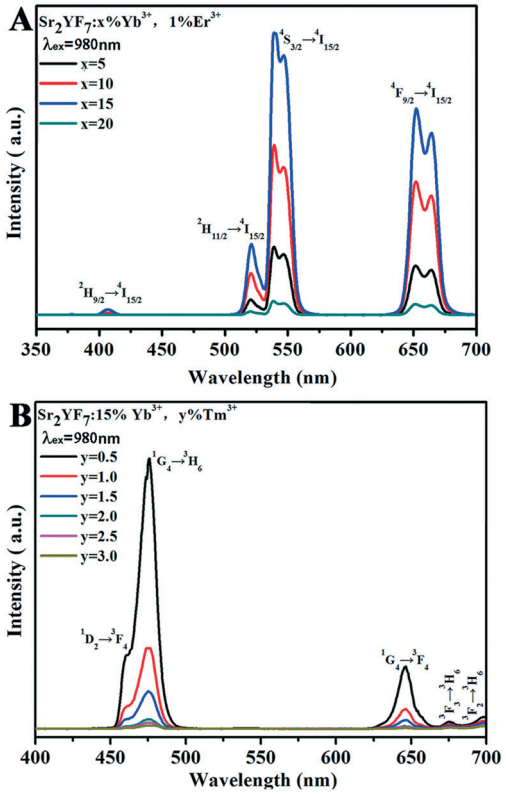

Fig. 10 UC emission spectra of Sr_2YF_7:x% Yb^{3+}/1% Er^{3+} (A) and Sr_2YF_7:15% Yb^{3+}/y% Tm^{3+} (B) under 980 nm excitation, respectively.

Yb^{3+}/0.5% Tm^{3+} samples display blue emission at 465 nm ($^1D_2 \rightarrow {}^3F_4$) and 476 nm ($^1G_4 \rightarrow {}^3H_6$) and the weaker red emission at 646 nm ($^1G_4 \rightarrow {}^3F_4$).

After a range of experiments about Sr_2YF_7:Yb^{3+}/Er^{3+} and Sr_2YF_7:Yb^{3+}/Tm^{3+} products, we observed that Sr_2YF_7:15% Yb^{3+}/0.5% Er^{3+} phosphors showed yellow light with a CIE color coordinate of (0.3705, 0.3835) and Sr_2YF_7:15% Yb^{3+}/0.5% Tm^{3+} showed blue light with a CIE color coordinate of (0.1612, 0.0961) in Fig. 11A-a and b, respectively. According to the color superposition principle, it is very possible to obtain UC white light by adjusting the appropriate doping content of Yb^{3+}/Er^{3+}/Tm^{3+} ions in the Sr_2YF_7 host. To prove our conjecture, a series of attempts were made next. First, we have synthesized Sr_2YF_7:15% Yb^{3+}/0.5% Er^{3+}/0.5% Tm^{3+} nanocrystals based on the previous reports.[55] It can be noted that the emission spectrum of the Sr_2YF_7:15% Yb^{3+}/0.5% Er^{3+}/0.5% Tm^{3+} sample (Fig. 11A-c) is composed of peaks at 465 nm and 476 nm due to the $^1D_2 \rightarrow {}^3F_4$ and $^1G_4 \rightarrow {}^3H_6$ transitions of Tm^{3+} ions in the blue region, green emissions at 522 nm and 540 nm from the $^2H_{11/2} \rightarrow {}^4I_{5/2}$ and $^4S_{3/2} \rightarrow {}^4I_{5/2}$ transitions as well as red emission at 652 nm ascribed to $^4F_{9/2} \rightarrow {}^4I_{5/2}$ of Er^{3+} ions, respectively. The red emission also involved the $^1G_4 \rightarrow {}^3F_4$ transition of Tm^{3+} ions at 646 nm despite its lower intensity, whose contribution in the red region can be neglected.[56] In addition, the sample of Sr_2YF_7:15% Yb^{3+}/0.5% Er^{3+}/0.5% Tm^{3+} shows white light with pale blue when viewed with naked eyes (Fig. 11A-c).

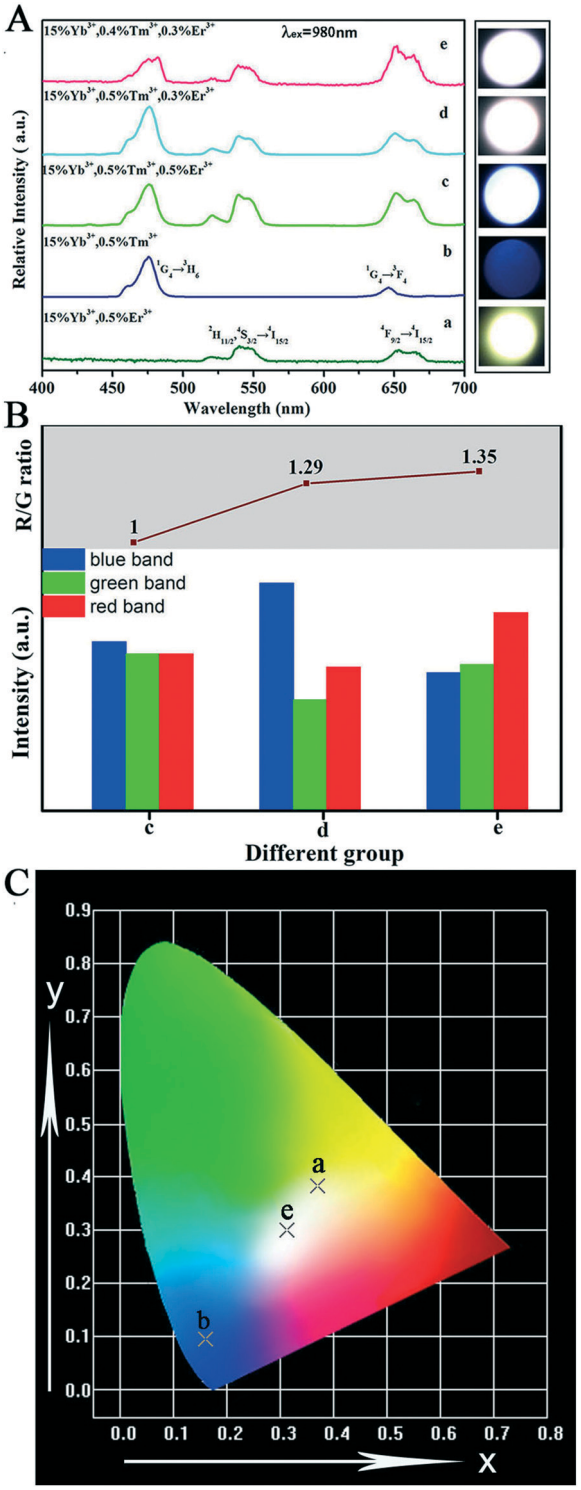

Fig. 11 (A) UC PL spectra of Sr_2YF_7:Yb^{3+}/Er^{3+}/Tm^{3+} and their corresponding luminescence photos under 980 nm excitation; (B) intensity ratios of RGB for the group c/d/e A; and (C) CIE chromaticity coordinates of group a/b/e in A.

It is well known that Yb^{3+} ions play an important role in sensitizing Er^{3+}/Tm^{3+} ions because of their larger absorption cross section at around 980 nm and longer excited state lifetime. The energy transfer generates as a result of the

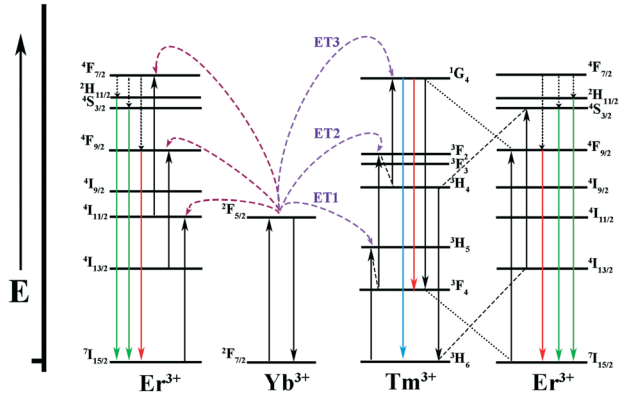

Fig. 12 Energy level diagrams of the Yb^{3+}, Er^{3+} and Tm^{3+} ions as well as the proposed UC mechanisms.

spectral overlap between the emission $^2F_{5/2} \rightarrow {}^2F_{7/2}$ of Yb^{3+} ions and the absorption $^4I_{11/2} \rightarrow {}^4I_{15/2}$ of Er^{3+} ions as well as the absorption $^3H_5 \rightarrow {}^3H_6$ of Tm^{3+} ions. As for Sr_2YF_7:Yb^{3+}/Er^{3+}, first of all, the photons are mostly absorbed by Yb^{3+} ions under excitation at 980 nm. It further transfers the energy to Er^{3+} ions to the $^4F_{7/2}$ level, which then relax to $^2H_{11/2}$, $^4S_{3/2}$ and $^4F_{9/2}$ levels by nonradiative relaxation. At last, the energy in these levels return to the ground state, resulting in green emissions at 522 nm and 540 nm ($^2H_{11/2} \rightarrow {}^4I_{5/2}$, $^4S_{3/2} \rightarrow {}^4I_{5/2}$) and red emission at 652 nm ($^4F_{9/2} \rightarrow {}^4I_{5/2}$). With respect to Sr_2YF_7:Yb^{3+}/Tm^{3+}, it has been proved that the energy transfer process between Yb^{3+} ions and Tm^{3+} ions is the three-photon process. First, the photons can be absorbed by the $^2F_{5/2}$ level of Yb^{3+}. Then, the nonresonant ET1 takes place to excite Tm^{3+} ions into the excited states $^3H_5$, relaxing subsequently to the $^3F_4$ state. The $^3F_4$ level of Tm^{3+} is excited into $^3F_2$ and $^3F_3$ levels by nonresonant ET2 process, and then Tm^{3+} ions return to the $^3H_6$ state. Finally, the nonresonant ET3 populates the $^1G_4$ level, which emits 474 nm ($^1G_4 \rightarrow {}^3H_6$) and 650 nm ($^1G_4 \rightarrow {}^3F_4$). The detailed energy level diagrams about Sr_2YF_7:Yb^{3+}/Er^{3+}, Yb^{3+}/Tm^{3+} and Yb^{3+}/Er^{3+}/Tm^{3+} are illustrated in Fig. 12.

The key to acquire the pure white light is properly enhancing the relative intensity of red emission.[12] The reduction of the green to red (G/R) ratio mainly concerns two energy transfer processes. One is the energy transfer from Er^{3+} ions to Yb^{3+} ions, resulting in the decrease of green ($^2H_{11/2}$, $^4S_{3/2} \rightarrow {}^4I_{5/2}$) emissions. Another is the transfer energy from excited Yb^{3+} ions to Er^{3+} ions, which can directly populate the $^4F_{9/2}$ level originating from $^2F_{5/2}(Yb^{3+}) + {}^4I_{13/2}(Er^{3+}) \rightarrow {}^2F_{7/2}(Yb^{3+}) + {}^4F_{9/2}(Er^{3+})$. However, some energy transfer processes between Er^{3+} ions and Tm^{3+} ions might also work in the complex system as follows: $^3H_4(Tm^{3+}) + {}^4I_{13/2}(Er^{3+}) \rightarrow {}^3H_6(Tm^{3+}) + {}^4S_{3/2}(Er^{3+})$; $^1G_4(Tm^{3+}) + {}^4I_{15/2}(Er^{3+}) \rightarrow {}^3F_4(Tm^{3+}) + {}^4F_{9/2}(Er^{3+})$. The ultraviolet emission is hardly detected in a tri-doped Sr_2YF_7 system according to the available conclusion.[10] In addition, the intensity ratios of the red to the green (R/G) emission increases gradually upon decreasing Tm^{3+} ions. Therefore, we conceived the idea of averaging the dopant concentrations of Er^{3+} ions and Tm^{3+} ions to obtain white light. The up-conversion emission spectra of Sr_2YF_7:Yb^{3+}/Er^{3+}/Tm^{3+} crystals with various concentrations of Er^{3+} and Tm^{3+} ions are shown in Fig. 11A-c–e. The relative intensity ratios of RGB were calculated by integral area of red band, green band and blue band from spectra.[57] From the corresponding information illustrated in Fig. 11B, we can directly observe the ratios of red band, green band and blue band of group c, d and e. The R/G ratio increases from 1 to 1.35 (inset of Fig. 11B). Ultimately, the target products Sr_2YF_7:15% Yb^{3+}/0.4% Tm^{3+}/0.3% Er^{3+} generate ideal UC white light, whose CIE color coordinate was calculated to be (0.3123, 0.3005) under a 980 nm pump with a power density of about 2 W cm^{-2}, as displayed in Fig. 11C (point e).

Conclusion

In summary, uniform and monodisperse Sr_2YF_7 spherical crystals have been successfully synthesized *via* a facile one-step hydrothermal route without any surfactant. We found that the pH values can change the morphology from spherical to octahedral shape and the various doped Ln^{3+} ions are beneficial to form different sizes of crystals ranging from 300 to 600 nm. The obtained Sr_2YF_7:Ln^{3+} (Ln = Dy, Tb, Eu, Tb/Eu, Yb/Er, Yb/Tm and Yb/Er/Tm) crystals show multicolor DS/UC luminescence properties. The energy transfer from Tb^{3+} ions to Eu^{3+} ions was observed in the Sr_2YF_7 host; the Sr_2YF_7:0.5% Dy^{3+} crystals show the nearly white emission under UV excitation at 217 nm; the ideal UC white light-emitting tri-doped Sr_2YF_7:15% Yb^{3+}/0.4% Er^{3+}/0.3% Tm^{3+} with a CIE color coordinate of (0.3123, 0.3005) was prepared under 980 nm excitation. In view of their simple production route and good properties, the Sr_2YF_7:Ln^{3+} materials may have potential applications in lighting, display devices and biological imaging.

Conflicts of interest

There are no conflicts of interest to declare.

Acknowledgements

This project is financially supported by the National Undergraduate Training Program for Innovation and Entrepreneurship of Southwest University, China (201710635040).

Notes and references

1 P. Du, X. Huang and J. S. Yu, *Chem. Eng. J.*, 2018, **337**, 91–100.
2 S. Sivakumar, F. C. J. M. van Veggel and M. Raudsepp, *J. Am. Chem. Soc.*, 2005, **127**(36), 12464–12465.
3 X. Chen, D. F. Peng, Q. Ju and F. Wang, *Chem. Soc. Rev.*, 2015, **44**, 1318–1330.
4 X. Hu, J. Gong, L. Zhang and J. C. Yu, *Adv. Mater.*, 2008, **20**(24), 4845–4850.

5 Y. Zhang, X. J. Li, Z. Y. Hou and J. Lin, *Nanoscale*, 2014, **6**, 6763–6771.
6 R. P. Cao, C. L. Liao, F. Xiao, G. T. Zheng, W. Hu, Y. M. Guo and Y. X. Ye, *Dyes Pigm.*, 2018, 574–580.
7 F. W. Kang, H. S. Zhang, L. Wondraczek, X. B. Yang, Y. Zhang, D. Y. Lei and M. Y. Peng, *Chem. Mater.*, 2016, **28**(8), 2692–2703.
8 M. Wang, C. C. Mi, W. X. Wang, C. H. Liu, Y. F. Wu, Z. R. Xu, C. B. Mao and S. K. Xu, *ACS Nano*, 2009, **3**, 1580–1586.
9 C. J. Boyer, F. Vetrone, A. L. Cuccia and A. J. Capobianco, *J. Am. Chem. Soc.*, 2006, **128**, 7444–7445.
10 Y. H. Yang, D. T. Tu, W. Zheng, Y. S. Liu, P. Huang, E. Ma, R. F. Li and X. Y. Chen, *Nanoscale*, 2014, **6**, 11098.
11 F. Auzel, *Chem. Rev.*, 2004, **104**, 139–174.
12 B. Zhao, D. Y. Shen, J. Yang, S. S. Hu, X. J. Zhou and J. F. Tang, *J. Mater. Chem. C*, 2017, **5**, 3264–3275.
13 Y. S. Liu, D. T. Tu, H. M. Zhu and X. Y. Chen, *Chem. Soc. Rev.*, 2013, **42**, 6924.
14 L. Xu, J. Shen, C. Lu, Y. Chen and W. Hou, *Cryst. Growth Des.*, 2009, **9**, 3129–3136.
15 Y. J. Ding, X. Teng, H. Zhu, L. L. Wang, W. B. Pei, J. J. Zhu, L. Huang and W. Huang, *Nanoscale*, 2013, **5**, 11928.
16 Z. Wang, J. Hao and H. L. W. Chan, *J. Mater. Chem.*, 2010, **20**, 3178.
17 M. Haase and H. Schafe, *Angew. Chem., Int. Ed.*, 2011, **50**, 5808.
18 G. Wang, Q. Peng and Y. Li, *Acc. Chem. Res.*, 2011, **44**, 322.
19 F. Wang, Y. Han, C. S. Lin, Y. Lu, J. Wang, J. Xu, H. Chen, C. Zhang, M. Hong and X. Liu, *Nature*, 2010, **463**, 1061.
20 B. Y. Chen, B. Dong, J. Wang, S. Zhang, L. Xu, W. Yu and S. W. Song, *Nanoscale*, 2013, **5**, 8541.
21 Z. L. Qiu, J. Shu and D. P. Tang, *Anal. Chem.*, 2018, **90**(1), 1021–1028.
22 Y. Zhang, D. L. Geng, X. J. Kang, M. M. Shang, Y. Wu, X. J. Li, H. Z. Lian, Z. Y. Cheng and J. Lin, *Inorg. Chem.*, 2013, **52**(22), 12986–12994.
23 V. Mahalingam, F. Vetrone, R. Naccache, A. Speghini and J. A. Colloidal Capobianco, *Adv. Mater.*, 2009, **21**, 4025.
24 Q. Liu, Y. Sun, T. S. Yang, W. Feng, C. G. Li and F. Y. Li, *J. Am. Chem. Soc.*, 2011, **133**, 17122.
25 Z. G. Xia, P. Du and L. B. Liao, *Phys. Status Solidi*, 2013, **210**(9), 1734–1737.
26 M. Ma, C. F. Xu, L. W. Yang, Q. B. Yang and J. G. Lin, *J. Alloys Compd.*, 2012, **525**, 97–102.
27 L. W. Han, S. S. Xie, M. Wang, T. M. Sun, Q. Liu, G. Q. Jiang, Y. J. Shi and Y. F. Tang, *Mater. Lett.*, 2019, 241–244.
28 Y. Ai, D. T. Tu, W. Zheng, Y. S. Liu, J. T. Kong, P. Hu, Z. Chen, M. D. Huang and X. Y. Chen, *Nanoscale*, 2013, **5**, 6430–6438.
29 A. Escudero, E. Moretti and M. Ocaña, *CrystEngComm*, 2014, **16**, 3274–3283.
30 J. Yang, Z. W. Quan, D. Y. Kong, X. M. Liu and J. Lin, *Cryst. Growth Des.*, 2007, **7**(4), 730–735.
31 X. D. Feng, Dean C. Sayle, Zhong Lin Wang, M. Sharon Paras, Brian Santora and A. C. Sutorik, *Science*, 2006, **312**(5579), 1504–1508.
32 C. X. Li, Z. W. Quan, P. P. Yang, S. S. Huang, H. Z. Lian and J. Lin, *J. Phys. Chem. C*, 2008, **112**, 13395.
33 R. Q. Li, L. L. Li, W. W. Zi, J. J. Zhang, L. Liu, L. C. Zou and S. C. Gan, *New J. Chem.*, 2015, **39**, 115–121.
34 B. Zhao, D. Y. Shen, J. Yang, S. S. Hu, X. J. Zhou and J. F. Tang, *J. Mater. Chem. C*, 2017, **5**, 3264–3275.
35 M. Wang, Q. L. Huang, J. M. Hong, X. T. Chen and Z. L. Xue, *Cryst. Growth Des.*, 2006, **6**, 2169.
36 X. Wang and Y. Li, *Angew. Chem., Int. Ed.*, 2002, **41**, 4790–4793.
37 D. Q. Chen and Y. S. Wang, *Nanoscale*, 2013, **5**, 4621–4637.
38 H. Cao, B. Xia, N. Xu and C. Zhang, *J. Alloys Compd.*, 2004, **376**(1–2), 282–286.
39 Y. S. Liu, D. T. Tu, H. M. Zhu and X. Y. Chen, *Chem. Soc. Rev.*, 2013, **42**, 6924.
40 B. Zhao, L. Yuan, S. S. Hu, X. M. Zhang, X. J. Zhou, J. F. Tang and J. Yang, *CrystEngComm*, 2016, **18**, 8044.
41 F. F. Chi, X. T. Wei, Y. G. Qin, F. Li, Y. H. Chen, C. K. Duan and M. Yin, *Phys. Chem. Chem. Phys.*, 2017, **19**, 12473–12479.
42 D. L. Geng, M. M. Shang, D. M. Yang, Y. Zhang, Z. Y. Cheng and J. Lin, *J. Mater. Chem.*, 2012, **22**, 23789–23798.
43 M. Yu, J. Lin, Z. Wang, J. Fu, S. Wang, H. J. Zhang and Y. C. Han, *Chem. Mater.*, 2002, **14**, 2224–2231.
44 J. Yang, C. X. Li, Z. W. Quan, C. M. Zhang, P. P. Yang, Y. Y. Li, C. C. Yu and J. Lin, *J. Phys. Chem. C*, 2008, **112**, 12777–12785.
45 X. F. Xu, J. X. Zhao, H. Feng, Z. C. Gao, L. Guan, Y. Yang, F. H. Wang, D. W. Wang and X. Li, *J. Lumin.*, 2020, **226**, 117356.
46 J. Yang, C. M. Zhang, C. X. Li, Y. N. Yu and J. Lin, *Inorg. Chem.*, 2008, **47**(16), 7262–7270.
47 Y. N. Mao, L. Jiang, R. Ye, J. Yang and S. S. Hu, *CrystEngComm*, 2020, **22**, 564–572.
48 W. P. Xia, Y. F. Zhang, J. Xiong, S. S. Hu, J. Yu, Y. F. Zhang, Y. X. Wan and J. Yang, *CrystEngComm*, 2019, **21**, 339–347.
49 L. Zhou, J. Yang, S. S. Hu, Y. Luo and J. Yang, *J. Mater. Sci.*, 2015, **50**, 4503–4515.
50 S. Li, N. Guo, Q. M. Liang, Y. Ding, H. T. Zhou, R. Z. Ouyang and W. Lü, *Spectrochim. Acta, Part A*, 2018, **190**, 246–252.
51 H. L. Li, G. X. Liu, J. X. Wang, X. T. Dong and W. S. Yu, *J. Lumin.*, 2017, **186**, 6–15.
52 E. J. Reszczyńska, T. Grzyb, J. W. Sobczak, W. Lisowski, M. Gazda, B. Ohtani and A. Zaleska, *Appl. Catal., B*, 2015, **163**, 40–49.
53 M. K. Gnanasammandhan, N. M. Idris, A. Bansal, K. Huang and Y. Zhang, *Nat. Protoc.*, 2016, **11**, 688–713.
54 J. Xie, J. X. Bin, M. Guan, H. K. Liu, D. X. Yang, J. G. Xue, L. B. Liao and L. F. Mei, *J. Lumin.*, 2018, **200**, 133–140.
55 H. L. Qiu, G. Y. Chen, L. Sun, S. W. Hao, G. Han and C. H. Yang, *J. Mater. Chem.*, 2011, **21**, 17202.
56 J. Yang, C. M. Zhang, C. Peng, C. X. Li, L. L. Wang, R. T. Chai and J. Lin, *Chem. – Eur. J.*, 2009, **15**, 4649–4655.
57 Q. B. Wu, S. T. Lin, Z. X. Xie, L. Q. Zhang, Y. N. Qian, Y. D. Wang and H. Y. Zhang, *Appl. Surf. Sci.*, 2017, **424**, 164–169.